Clinical & Experimental Metastasis (2025) 42:19
https://doi.org/10.1007/s10585-025-10336-3

RESEARCH PAPER

A novel optimized orthotopic mouse model for brain metastasis with sustained cerebral blood circulation and capability of multiple delivery

Zihao Liu[1] · Huisheng Song[2] · Zhenning Wang[3] · Yang Hu[1] · Xiaoxuan Zhong[4] · Huiling Liu[5] · Jianhao Zeng[6] · Zhiming Ye[1] · Wenfeng Ning[7] · Yizhi Liang[4] · Shengfang Yuan[1] · Zijun Deng[1] · Long Jin[4] · Jieying Mo[1] · Jiaoyan Ren[8] · Maojin Yao[1]

Received: 4 June 2024 / Accepted: 26 February 2025

Abstract

Brain metastasis is thought to be related to the high mortality and poor prognosis of lung cancer. Despite significant advances in the treatment of primary lung cancer, the unique microenvironment of the brain renders current therapeutic strategies largely ineffective against brain metastasis. The lack of effective drugs for brain metastasis treatment is primarily due to the incomplete understanding of the mechanisms underlying its initiation and progression. Currently, our understanding of brain metastasis remains limited, primarily due to the absence of appropriate models that can realistically simulate the entire process of tumor cell detachment from the primary site, circulation through the bloodstream, and eventual colonization of the brain. Therefore, there is a pressing need to develop more suitable lung cancer brain metastasis models that can effectively replicate these critical stages of metastasis. Here, based on the traditional carotid artery injection model, we established a novel orthotopic mouse model by using a light-controlled hydrogel to repair the puncture site on the carotid artery, with sustained cerebral blood circulation and the capability of multiple delivery cancer cell to mimic lung cancer brain metastasis. The optimized orthotopic mouse model significantly reduced cerebral ischemia and improved cerebral oxygenation by 60% compared to the traditional orthotopic mouse model, enhancing post-operative survival rates. It also showed a reduction in pro-inflammatory cytokines and featured less inflammatory and more resting states of microglial and astrocyte cells. Furthermore, the optimized orthotopic mouse model markedly increased the success rate and absolute number of the metastatic clones in the brain. Additionally, the multiple delivery model based on the optimized orthotopic mouse model substantially augmented the tumor clone number and formation rates compared to single injection in the optimized orthotopic mouse model. This model overcomes previous limitations by maintaining cerebral circulation, providing a more accurate simulation of the continuous entry of tumor cells into cerebral circulation. It offers a robust platform for studying the interactions of cancer cells with the brain microenvironment and testing new therapeutic approaches.

Zihao Liu and Huisheng Song contributed equally to this work.

Extended author information available on the last page of the article

Published online: 17 March 2025

Graphical abstract

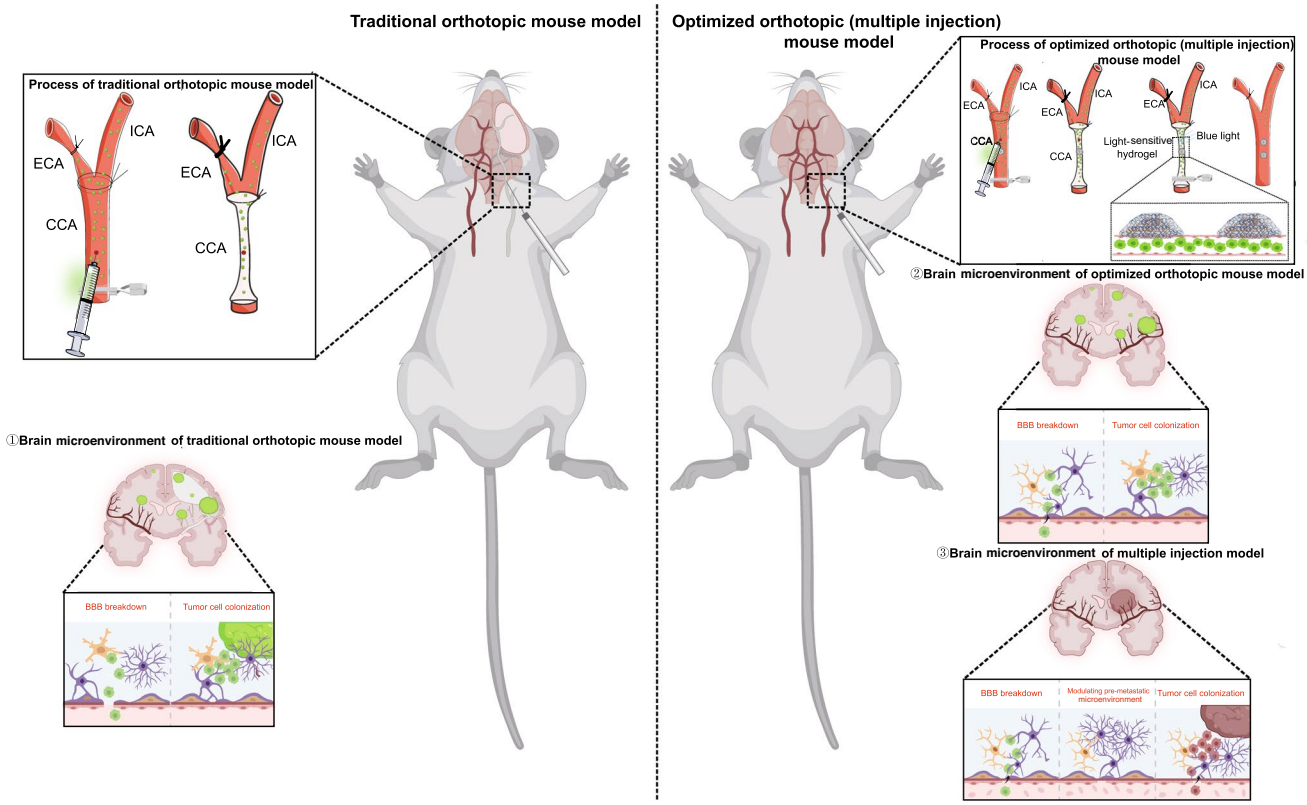

Keywords Non-small cell lung cancer · Brain metastasis · Orthotopic model · Animal model · Hemodynamic · Tumor microenvironment

Background

Brain metastases from lung cancer represent a critical and increasingly common complication that significantly impacts mortality of lung cancer patients [1, 2]. Disappointingly, current treatment strategies face significant hurdles, particularly due to the brain's unique environment and the blood–brain barrier (BBB), which limits the efficacy of systemic therapies [3, 4].

Understanding the complex interactions between the metastatic cancer cells and the brain's microenvironment is critical for developing effective therapeutics [5]. Lung cancer brain metastasis is a complex process that begins when endoderm-derived lung cancer cells regain stem cell-like characteristics, enabling them to acquire migratory abilities and breach the lung tissue barrier to intravasate into the circulatory system [6, 7]. Once in the bloodstream, these cells need to survive evade the immune system's defenses and the shear forces of blood flow [8, 9]. The key to tumor cell colonization in the brain is endoderm-derived tumor cells adapt to an environment enriched with ectoderm-derived neurons and glial cells [10, 11]. The ability of endoderm-derived lung cancer cells to settle and thrive in the ectoderm-derived brain tissue highlights the remarkable plasticity and adaptive mechanisms of cancer cells [12]. Studying these processes could also unveil critical insights into how disparate embryonic tissues interact at a molecular level during disease progression and offer potential therapeutic targets to hinder or prevent brain metastasis in lung cancer patients.

The most commonly used model for lung cancer brain metastasis research is the traditional orthotopic mouse model (TOMM), in which lung cancer cells are injected via common carotid artery (CCA), allowing the cells to enter the brain circulation accurately. This model offers advantages such as high tumor take rates and short tumorigenesis time. However, the TOMM model requires permanent ligation of the CCA, which prevents it from simulating the diffusion process of circulating tumor cells under intact blood flow shear forces and cerebral hemodynamics [13]. Most

importantly, TOMM is unable to simulate the continuous entry of tumor cells into the cerebral circulation, hence they fail to study the impact of pioneer tumor cells on the brain microenvironment and the subsequent effects on the colonization of subsequent tumor cells in the brain.

Further optimization of brain metastasis orthotopic mouse model with sustained cerebral blood circulation can significantly advance research in this field. First, a model with intact cerebral hemodynamics would allow for the study of how cancer cells breach the BBB, a key step in brain metastasis. Second, maintaining cerebral hemodynamics ensures a more authentic interaction between the tumor cells and the brain's microenvironment, which is crucial for understanding tumor behavior and progression. Third, intact hemodynamics allow for the exploration of how blood flow patterns and vascular architecture in the brain affect metastatic spread and tumor growth, leading to more accurate and translatable findings. Fourth, a model that accurately replicates cerebral blood flow and BBB dynamics can be used to test the efficacy of drugs and their ability to penetrate the brain, leading to better therapeutic strategies.

Here, we describe a novel orthotopic brain metastasis mouse model that utilized a light-controlled hydrogel to repair CCA and achieved sustained cerebral blood circulation and the capability of multiple cancer cell deliveries. Hydrogels, particularly gelatin methacryloyl (GelMA), have significant applications in tissue repair due to their biocompatibility [14]. By incorporating hyaluronic acid (HA), GelMA-based hydrogels exhibit enhanced properties, including promoting cell proliferation and angiogenesis, essential for tissue regeneration [15]. To address the challenge of permanent CCA ligation in the TOMM, we developed a novel orthotopic brain metastasis mouse model using a light-controlled GelMA/HAMA hydrogel, which, activated by 405 nm blue light, effectively repairs the puncture site and maintains normal blood flow. This optimized model satisfies the aforementioned requirements to recapitulate the interaction between metastatic cancer cells and brain microenvironment.

Methods

Synthesis of methacrylated gelatin (GelMA)

GelMA was prepared according to the previous method [16]. Weighing 20 g gelatin was dissolved in 250 ml ultrapure water at 60 °C. Then, 12 ml of MA was added dropwise into the gelatin solution. After stirring for 12 h at 37 °C, the solution was dialyzed in a dialysis bag (3500 Da molecular weight cutoff) against ultrapure water for 3 days. Then, the solution was freeze-dried to obtain GelMA polymer and stored at − 20 °C for future use.

Synthesis of methacrylated hyaluronic acid (HAMA)

HAMA was prepared as previously described with slight modification [17]. Weighing 1 g of HA was stirred in 100 ml of ultra-pure water until completely dissolved. Then, 3 ml of MA was added dropwise into the hyaluronic acid solution and stirred for 8 h at room temperature (pH was kept at about 8.5 by adding 5 mol/l sodium hydroxide). Finally, the reaction mixture was dialyzed in a dialysis bag (MWCO 8–14 kDa) against ultra-pure water for 3 days. The resulting solution was freeze-dried to obtain HAMA polymer and stored at − 20 °C for further use.

Preparation of composite hydrogels

The freeze-dried GelMA and HAMA were dissolved in phosphate-buffered saline (PBS) at 60 ° C to make the final GelMA concentrations of 10% (w/v) with HAMA concentrations of 0.5% (w/v). Then, 0.1% (w/v) photoinitiator LAP was added, and the prepolymer solution was then exposed to the UV light (365 nm) for 30 s.

Cell line and culture

Human Non-small cell lung cancer (NSCLC) cell lines, A549, PC9, originally from American Type Culture Collection, were cultured in accordance with standard requirements. A549 was cultured in DMEM (HyClone, USA) supplemented with 10% FBS (HyClone, USA) and 1% Penicillin–Streptomycin (Gibco, USA). PC9 was cultured in RPMI 1640 (HyClone, USA) supplemented with 10% FBS and 1% Penicillin–Streptomycin. All cells were cultured in a humidified atmosphere containing 5% CO_2 at 37 °C. All cell lines were mycoplasma free and routinely tested by PCR.

Stable cell transfection

A549 and PC9 cells stably expressing green fluorescent protein (GFP) were generated for functional studies. For the production of lentiviral particles, 293 T cells were co-transfected with 5 μg of lentiviral vectors pLenti-C-mGFP-P2A-Puro (Origene, PS100093), 5 μg of pMD2-VSV-GENV, 2.5 μg of pRSV-Rev, 2.5 μg of pMDLg/pRRE by using the calcium phosphate method. After 48 h, the supernatant containing lentiviral particles was recovered, ultracentrifuged at 19,800 rpm using an SW28 rotor for 2 h, and resuspended in PBS (500 μL for 20 ml of supernatant). A549 and PC9 cells were infected with 80 μL of viral suspension in a medium supplemented with polybrene (4 μg/mL) for 8 h. Two consecutive rounds of infections were performed to improve the efficiency.

Animals

All studies were approved by the Guangzhou Medical University Committee for Animal Use and Welfare (ethical approval number:2023395). Nod-SCID female mice were purchased from GemPharmatech Co., Ltd. Animals were housed under standard vivarium conditions (22 ± 1 °C, 12 h light/dark cycle, with ad libitum food and water).

Anesthesia and injection procedures

After a habituation period of 1 week, the mice were administered 5% isoflurane for anesthesia induction and 1.5% isoflurane for anesthesia maintenance in 30% O_2/70% N_2 through a facemask. Each mouse was placed in the supine position and fixed on an operating table. The middle of the neck was sterilized, and one small incision was made. The right common carotid artery was isolated, ensuring separation from the vagus nerve. The 8–0 sutures were placed at the proximal and distal ends of the exposed carotid artery. The proximal suture was tied first, and the artery was punctured using a microsyringe for cell injection. The cells were slowly injected from the syringe into the carotid artery. It is crucial to avoid introducing air bubbles into the blood vessels, as this could cause air embolism and result in the death of the mouse. Successful injection can be observed under the microscope by the changing color of nearby blood vessels and musculature when buffered cancer cells are pushed into the circulation. After cell injection, the distal suture was gently lifted to prevent tumor cell reflux. The syringe needle was then removed, and the distal suture was quickly ligated. Subsequently, a light-controlled hydrogel was rapidly implanted, covering the puncture site of the CCA. Blue light was applied to the hydrogel to solidify it. Once the hydrogel solidified, the distal suture was first released, ensuring no bleeding, followed by the release of the proximal suture. Finally, the skin was sutured using 3–0 sutures. The key steps of the injection procedures are shown in the video in Supplementary Video 1.

2,3,5-Triphenyl tetrazolium chloride (TTC) staining

Two hours after the modeling, mice in the different models were sacrificed for the assessment of brain hypoxic conditions. The brain was removed from the skull, placed in a brain matrix, and sliced into 1 mm coronal sections. The slices were incubated in 2% TTC (Sigma-Aldrich, USA) solution at 37 °C for 10 min and then stored in 4% paraformaldehyde for 24 h for later visualization. The brain slices was digitally imaged using a stereo zoom microscope (Axio Zoom.V16, ZEISS, Germany).

Photoacoustic imaging (PAI) system

The brain microvessels of mice after different models were imaged by an optical resolution PAI system at 532 nm. In brief, after the mouse model was successfully established, the scalp of the mouse was opened by scissors. Then the brain area of the mouse was placed in the system for scanning.

The laser repetition rate of the system was 5 kHz with a pulse width of 7 ns. The acoustic signals generated by laser irradiation on the imaging tissues were amplified by a 50-dB amplifier (Mini-Circuits, USA) and then received by a 50 MHz ultrasonic sensor. The maximum amplitude projection images of the ROI were acquired by integrating the signals with the computer.

Tissue preparation and immunostainings

To collect mouse brain used for cryosection, after anesthesia, mice were briefly perfused with cold PBS and then with 4% paraformaldehyde. The brains were then isolated and post-fixed in 4% paraformaldehyde for 24 h and dehydrated in 30% sucrose for 48 h. Fixed brain tissues were embedded into Optimal Cutting Temperature compound (SAKURA, USA). The embedded brains were cut into frozen sections of 25 μm thickness in series on CT520 (Dakewe Biotech Co., Ltd.).

The following primary antibodies were used for immunofluorescent staining: anti-Glial fibrillary acidic protein (GFAP) (DAKO, catalog #53554, dilution 1:500); anti-Ionized calcium-binding adaptor molecule 1 (IBA-1) (Abcam, catalog #ab5076, dilution 1:250). The following secondary antibodies were used for immuno-fluorescent staining: Alexa Fluor 488 donkey anti-rabbit (Invitrogen, catalog #A21206, dilution 1:250); Alexa Fluor 488 donkey anti-goat (Invitrogen, catalog #A11055, dilution 1:250); Alexa Fluor 555 donkey anti-rabbit (Invitrogen, catalog #A31572, dilution 1:250); Alexa Fluor 555 donkey anti-goat (Invitrogen, catalog #A21432, dilution 1:250); Alexa Fluor 647 donkey anti-rabbit (Invitrogen, catalog #A31573, dilution 1:250); Alexa Fluor 647 donkey anti-goat (Invitrogen, catalog #A21447, dilution 1:250).

Imaging

Tumor cells' location in brain were monitored by a fluorescence stereo zoom microscope (Axio Zoom.V16, ZEISS, Germany). After staining was completed, fluorescence images were obtained using a fluorescence microscope (Leica DM6, Germany) and a confocal laser-scanning microscope (LSM880, ZEISS, Germany).

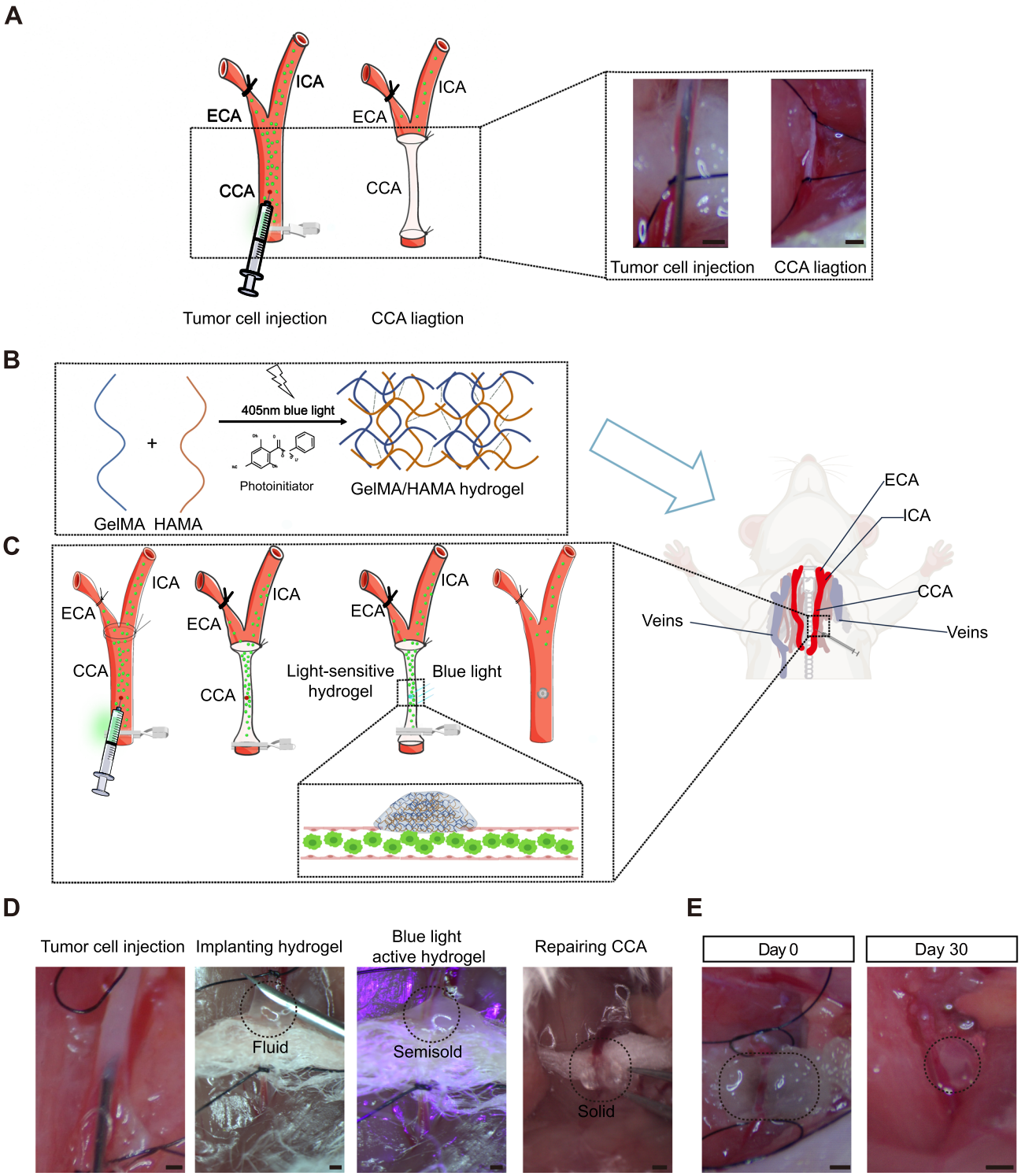

Fig. 1 An optimized orthotopic mouse model for cancer brain metastasis with sustained cerebral blood circulation. **A** Schematic illustration of the TOMM and images depicting various stages of the TOMM process. Scale bar = 2 mm. **B** Schematic illustration of the preparation of GelMA/HAMA. **C** Schematic illustration of the OOMM process and the role of GelMA/HAMA in repairing the CCA. **D** Images depicting various stages of the OOMM process and GelMA/HAMA application. Scale bar = 2 mm. **E** Images showing the CCA injection site following GelMA/HAMA application at day 0 and day 30. Scale bar: 2 mm

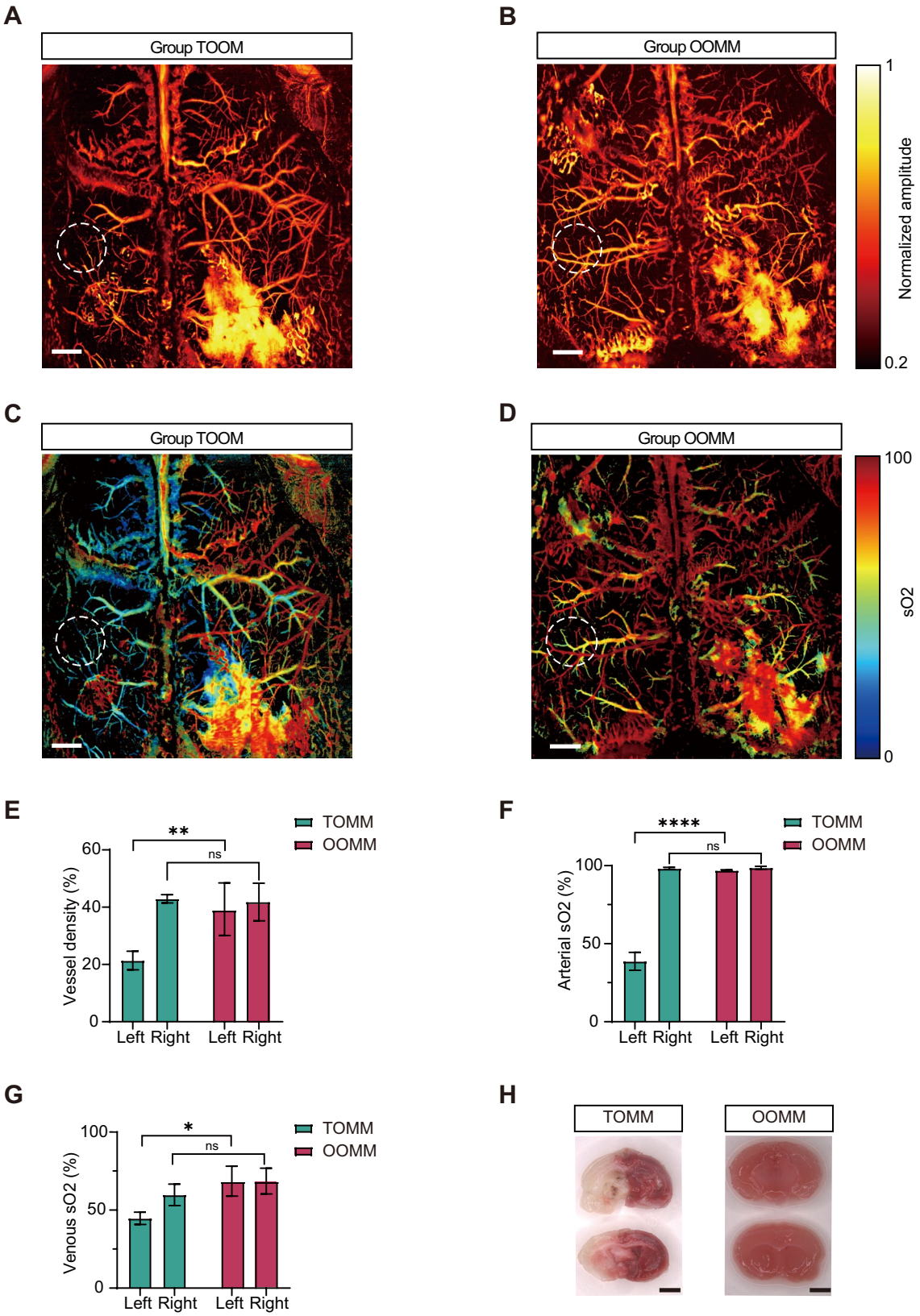
A
Group TOOM
B
Group OOMM
1
Normalized amplitude
0.2
C
Group TOOM
D
Group OOMM
100
sO2
0
E
TOMM
OOMM
**
ns
Vessel density (%)
60
40
20
0
Left Right Left Right
F
TOMM
OOMM
****
ns
Arterial sO2 (%)
100
50
0
Left Right Left Right
G
TOMM
OOMM
*
ns
Venous sO2 (%)
100
50
0
Left Right Left Right
H
TOMM
OOMM

◂**Fig. 2** The analyses of mouse brain hemodynamic and oxygen saturation treated with TOMM and OOMM. Photoacoustic imaging of the blood flow in the brain of **A** TOMM-treated mice, **B** OOMM-treated mice. Photoacoustic imaging of oxygen saturation in the brain of **C** TOMM-treated mice, **D** OOMM-treated mice. Quantification of **E** blood vessel density, **F** arterial oxygen saturation and **G** venous oxygen saturation in left and right side of the brain in mice after the TOMM and OOMM procedure. Data are presented as mean ± SD from $n = 3$ mice. * < 0.05, ** < 0.01, **** < 0.0001 by paired t test. **H** Representative images of cerebral infraction in mice treated with the TOMM or the OOMM procedures. TTC staining was performed with brain slides. $n = 3$ mice for each group. Scale bar: **A**–**D** 2 mm; **H** 2 mm

Cytokine determination by magnetic multiplex assay

Mouse brain tissue was analyzed for cytokines using the Magnetic Luminex Performance Assay (R&D Systems). MAGPIX (Luminex, USA) was used to read the multiplex assay. As with the enzyme-linked immunosorbent assay (ELISA), all sample time points for a given individual were assayed within the same sample plate; only one assay plate was run.

Statistical analysis

Statistical analysis was performed using GraphPad Prism 9. Comparisons of two groups were performed by paired t test. Comparisons of more than two groups were performed using a one-way ANOVA with Dunnett's multiple comparison post hoc test. The number of mice and samples, and the specific statistical tests performed, are indicated in the figure legends. Differences in means were considered statistically significant at *, $p < 0.05$; **, $p < 0.01$; ***, $p < 0.001$; ****, $p < 0.0001$.

Results

Optimized orthotopic mouse model

In TOMM, a puncture is made in the CCA by injecting tumor cells. To prevent bleeding and the backflow of tumor cells at the puncture site, the CCA is permanently ligated (Fig. 1A). However, this also disrupts normal blood flow to the brain, potentially leading to ischemia in the areas of the brain that the artery supplies. This alteration in blood supply can also affect the physiological state of the brain, potentially influencing the behavior of both tumor and brain microenvironment cells. To circumvent the issues caused by CCA ligation, we synthesized a light-controlled hydrogel GelMA/HAMA, which can be activated by 405 nm blue light initiating a second crosslinking phase to repair the puncture site, to sustain the normal blood flow (Fig. 1B, C). The characterizations of the GelMA/HAMA hydrogels can be seen in supplementary Fig. 1. During the injection process, the light-controlled hydrogel is implanted near the injection site. Subsequently, a blue light flashlight is used to stimulate the light-controlled hydrogel, inducing a second crosslinking phase. This transition gradually changes the light-controlled hydrogel from a liquid to a solid state, effectively repairing the CCA (Fig. 1D). Given the application of light-controlled hydrogel for arterial injection site repair, it is crucial that its structure within be robust and non-absorbable. It is observable that the light-controlled hydrogel remains stably attached to the injection site after 30 days of implantation (Fig. 1E). We established a novel brain metastasis orthotopic mouse model by using a light-sensitive GelMA/HAMA hydrogel, which solidifies under blue light to repair the puncture in CCA, thereby maintaining physiological brain function and potentially offering a more suitable model for investigating tumor cell behavior and interactions with the brain microenvironment. The hydrogel remains stable and effective for a long time post-application.

OOMM model shows significantly improved cerebral blood flow and oxygen supply

To explore whether the OOMM model without the ligation of CCA after tumor cell grafting can improve the cerebral oxygen supply compared to TOMM, whole-brain photoacoustic imaging scans were performed 2 h after surgery in both models. The TOMM showed a significant reduction in cerebral blood flow signal due to permanent closure of the common carotid artery, while the OOMM showed a reduction in some cerebral capillary blood flow signals likely due to temporary closure of the common carotid artery (Fig. 2A vs. B). The base-line of blood flow and oxygen saturation in photoacoustic imaging can see in supplementary Fig. 2. Spectral analysis of changes in blood oxygen content within brain vessels showed that the traditional model had a significantly reduced blood oxygen signal in the cerebral cortex, whereas the improved model showed a reduction in blood oxygen signals in small vessels in the cerebral cortex (Fig. 2C VS. D). There was a statistically significant difference between the two models in left cerebral vessel density signals intensity (Fig. 2E). The difference in oxyhemoglobin saturation in the left cerebral artery between the two models was statistically significant, and there was also a difference in venous oxyhemoglobin saturation in the left cerebrum between the two models (Fig. 2F, G). To explore the oxygenation status of the whole brain, especially the deeper locations, we utilized 2,3,5-Triphenyl tetrazolium chloride (TTC) staining to analyze the hypoxic conditions in the brain tissues of both model groups. TTC staining of mouse brains was performed 2 h after modeling. The white areas represent ischemic and hypoxic tissues, and the red

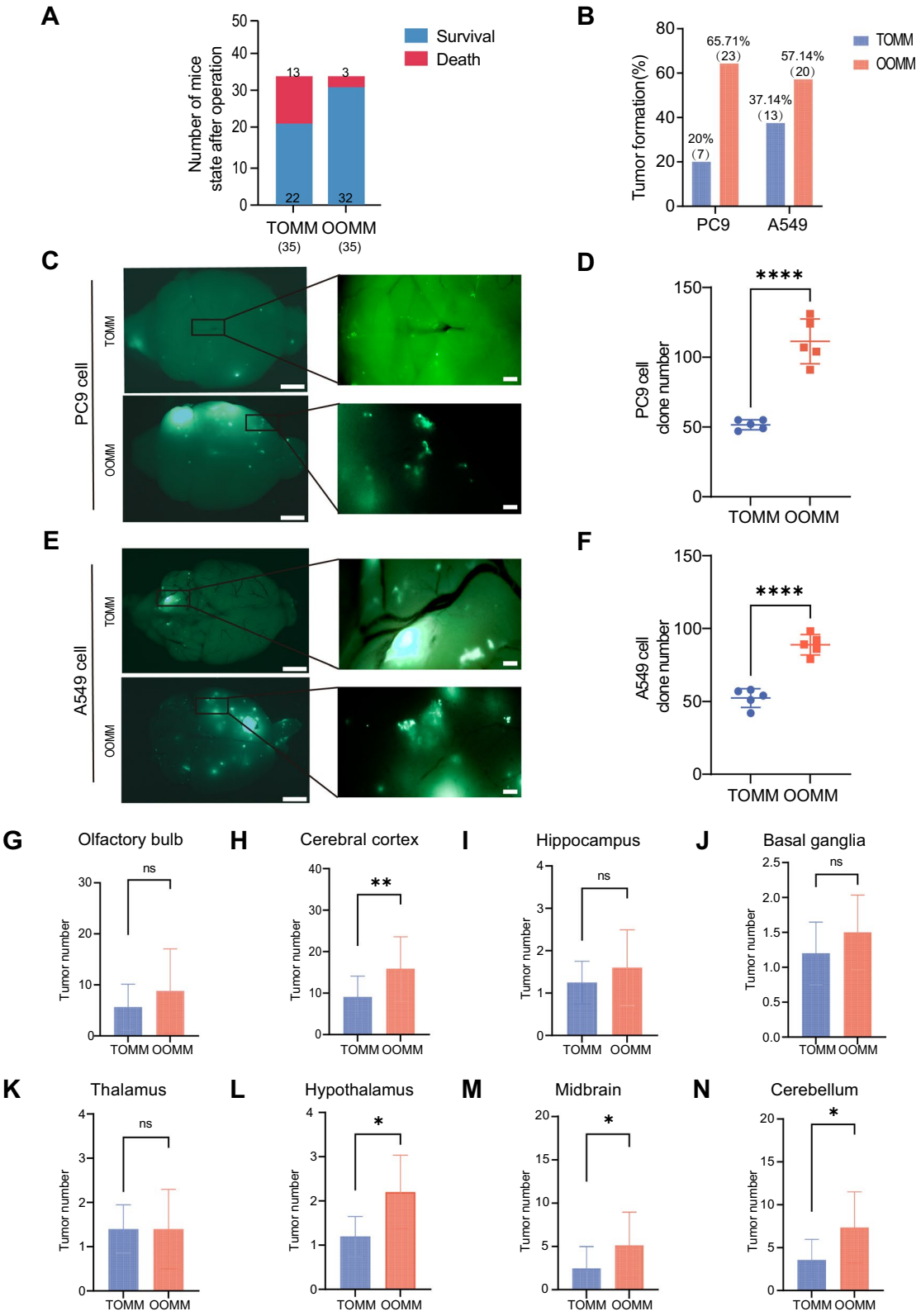
A
Number of mice state after operation
Survival
Death
13
3
22
32
TOMM OOMM
(35) (35)
B
Tumor formation (%)
TOMM
OOMM
65.71% (23)
57.14% (20)
37.14% (13)
20% (7)
PC9
A549
C
PC9 cell
TOMM
OOMM
D
PC9 cell clone number
****
TOMM OOMM
E
A549 cell
TOMM
OOMM
F
A549 cell clone number
****
TOMM OOMM
G
Olfactory bulb
Tumor number
ns
TOMM OOMM
H
Cerebral cortex
Tumor number
**
TOMM OOMM
I
Hippocampus
Tumor number
ns
TOMM OOMM
J
Basal ganglia
Tumor number
ns
TOMM OOMM
K
Thalamus
Tumor number
ns
TOMM OOMM
L
Hypothalamus
Tumor number
*
TOMM OOMM
M
Midbrain
Tumor number
*
TOMM OOMM
N
Cerebellum
Tumor number
*
TOMM OOMM

◂**Fig. 3** The OOMM demonstrates improved post-procedure survival rate of mice, elevated tumor clone formation, and an altered spatial distribution of tumor clones when compared to TOMM. **A** The post-procedure survival rate of mice 24 h after the TOMM or the OOMM procedure. **B** The success rate of metastatic brain tumor formation following the TOMM or the OOMM procedure. Representative image of the formation of tumor clones (green, GFP+) in the mouse brain 45 days post the TOMM or the OOMM procedure. **C** PC9 cells; **E** A549 cells. Scale bar: left column 2 mm; right column 10 mm. Quantification of the number of tumor clones per brain from mice treated with the TOMM or the OOMM procedure: **D** PC9 cells; **F** A549 cells. Data are presented as mean ± SD from $n = 5$ mice. **** < 0.0001 by paired t test. **G** Spatial distribution of PC9 cell line tumor clone in the brain of mice treated with the TOMM or the OOMM procedure. Data are presented as mean ± SD from $n = 7$ mice in TOMM group, $n = 23$ mice in OOMM group. * < 0.05, ** < 0.01 by paired t test

areas represent normally perfused tissues. It was found that the OOMM significantly ameliorated cerebral ischemia and hypoxia compared to the TOMM (Fig. 2H).

OOMM model demonstrates enhanced success rate of brain metastasis

The assessment of tumor clone numbers indicates the capability of cancer cells to proliferate and form new lesions in brain metastasis models. Models yielding numerous tumor clones are more valuable for lung cancer brain metastasis research, closely mirroring the complexity of human disease. An increase in tumor clone numbers suggests the model provides conducive conditions for tumor cell growth and proliferation. We evaluated the differences between the optimized model and the traditional model in three aspects: survival rates of mice 24 h post-surgery, tumorigenesis rates six weeks after surgery, and the number of brain metastatic tumors. Initially, we assessed the survival of mice within 24 h post-modelling for both the traditional and optimized models. Due to improved cerebral cortical vascular blood flow and oxygen content, the optimized model showed a significantly reduced post-surgery mortality. In the optimized model group, 32 out of 35 mice survived (94%); whereas in the traditional model group, only 22 out of 35 mice survived (63%) (Fig. 3A). It is noteworthy that our experimental data indicate that survival rates in the OOMM model were lower for C57BL/6 mice (immunocompetent mice) compared to NOD-SCID mice (data not shown). This difference may be attributed to the weaker immune response in NOD-SCID mice. We used the *Epidermal growth factor receptor (EGFR)* mutated PC9 cell line and the *Khirsten RNA associated rat sarcoma 2 virus (Kras)* mutated A549 cell line for tumor grafting, as *EGFR* and *Kras* are the most common driver genes in lung cancer brain metastasis. In the traditional model, the tumor formation rate was 20% for PC9 cells and 37.14% for A549 cells. In contrast, in the improved model, the tumor formation rate increased to 64.71% for PC9 cells and 57.14% for A549 cells (Fig. 3B), underscoring a higher repeatability of our optimized model for brain metastasis. Regarding the abundance of metastatic tumor clones in each mouse, PC9 cells in the improved model had significantly more brain metastatic tumors than in the traditional model, and the difference in the number of tumors between the two models for PC9 cells was statistically significant (Fig. 3C, D). Consistently, A549 cells in the improved model had significantly more brain metastatic tumors than in the traditional model, and the difference in the number of tumors between the two models for A549 cells was statistically significant (Fig. 3E, F). The conventional lung cancer brain metastasis model, including the intracardiac and tail vein injection models, formed fewer tumor clones in the brain and produced a large number of pulmonary tumor clones (Supplementary Fig. 3A, B). The number of intracranial tumor clones formed in both the intracardiac and tail vein injection models was significantly lower than that in the OOMM, with a statistically significant difference (Supplementary Fig. 3C, D).

Additionally, we assessed the spatial distribution of the metastatic tumor clones in different brain regions between the two models. The olfactory bulb (Fig. 3G) shows no significant difference between the models, indicating a similar propensity for tumor formation in this brain region across both models. In contrast, the cerebral cortex (Fig. 3H) exhibits a marked difference, suggesting a variance in tumor distribution likely influenced by the blood supply from the CCA, which predominates in this area. A significant increase in tumor numbers was observed in the Hypothalamus (Fig. 3L), Midbrain (Fig. 3M), and Cerebellum (Fig. 3N) in the OOMM model compared to TOMM. Thalamus (Fig. 3K) and Hippocampus (Fig. 3I) exhibit no significant change.

The study's assessment of tumor clone numbers revealed crucial insights into the proliferation and lesion formation abilities of cancer cells in models of brain metastasis. The optimized model, with improved survival rates and higher tumorigenesis rates, outperformed the traditional model, indicating a more conducive environment for tumor growth and a more accurate reflection of the human disease state.

Impact of intact cerebral blood flow on tumor cell distribution and metastasis in brain

To study the impact of cerebral blood flow on the distribution of brain metastatic cells and the differences in tumor formation between the two models, we employed two injection methods and collected mouse brain tissues at three time points: 12 h, day 7, and day 14 post-surgery.

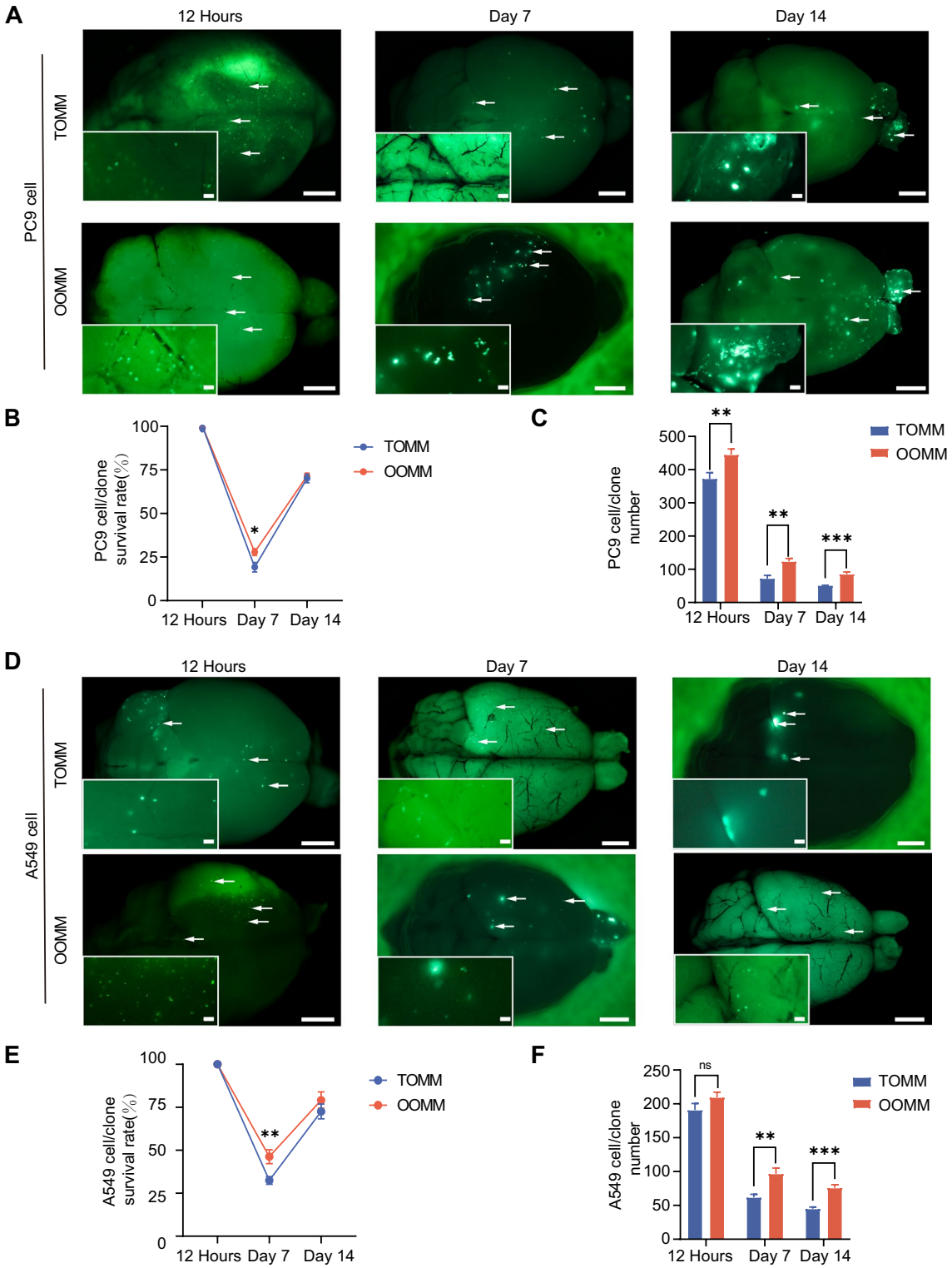

Fig. 4 OOMM extended survival of cancer cells in the mouse brain. Stereoscopic fluorescence imaging of whole mouse brain to detect survival tumor cells at 12 hour, day 7, and day 14 post the TOMM or the OOMM procedure: **A** PC9 cells; **D** A549 cells. Scale bar: **C** and **D** 2 mm, insets 10 mm. Quantification of tumor clone survival rate at 12 hour, day 7, and day 14 post the TOMM or the OOMM procedure: **B** PC9 cells; **E** A549 cells. Data are presented as mean ± SD from $n = 3$ mice. *** < 0.001 by paired t test. Quantification of tumor clone number at 12 hour, day 7, and day 14 post the TOMM or the OOMM procedure: **C** PC9 cells; **F** A549 cells. Data are presented as mean ± SD from $n = 3$ mice. ** < 0.01, *** < 0.001 by paired t test

Twelve hours after injection, PC9 cells in the OOMM were uniformly distributed throughout the brain, whereas in the TOMM, cells were confined to specific regions such as the olfactory bulb, cortex, hippocampus, basal ganglia, thalamus, and hypothalamus. After seven days, the TOMM exhibited weakened fluorescence signals, while the OOMM displayed stronger and larger signals, suggesting better survival and possible proliferation of PC9 tumor cells at this time point. After fourteen days, the TOMM barely showed any visible punctate fluorescence, with only clumped fluorescence signals remaining, possibly indicating that most tumor cells did not survive long-term, and only a fraction capable of proliferation formed large clones. In contrast, the optimized model not only showed clumped fluorescence but also retained some small punctate signals, suggesting not only did the tumor cells survive and regain proliferative capacity to form large metastatic foci but also some cells might be in a dormant state (Fig. 4A). To quantify tumor cell survival, we used fluorescence stereomicroscopy to count the number of tumor cells/clones at 12 hour, day 7, and day 14 post-injection. The 12 hour count served as the baseline, and survival rates were calculated by dividing the number of tumor cells/clones at day 7 and day 14 by the respective numbers at earlier time points. The survival rate of PC9 tumor cell clone initially decreases and then increases in both models, with significant statistical differences in tumor clone survival rate between the two models at the day 7 (Fig. 4B). Over time, the number of clones formed in both the optimized and traditional models decreased (Fig. 4C).

Twelve hours after injection, A549 cells fluorescence signals were scarcely visible in the TOMM, while the OOMM showed a robust punctate fluorescence signal. By day seven, fluorescence signals from A549 cells in the TOMM had declined but were still detectable. In contrast, the OOMM showed denser fluorescence with larger spots, indicating better survival and proliferation conditions for A549 cells. After fourteen days, the OOMM showed more fluorescence spots compared to the traditional model, especially in the olfactory bulb, suggesting a significant increase in tumor activity (Fig. 4D). Also, the survival rate of A549 tumor cell clone initially decreased and then increases in both models, with significant statistical differences in tumor clone survival rate between the two models at the day 7 (Fig. 4E). Similarly, the number of clones formed by A549 cells in both the optimized and traditional models decreased over time (Fig. 4F).

OOMM model reduced activation of astrocytes and microglia

Cytokines are direct executors of immune responses and can be detected for significant changes in their quantity in the early stages of inflammation. Therefore, we used the luminex high-sensitivity cytokine detection method to compare the inflammation response in TOMM and OOMM. Although elevated cytokines were found in both models 12 h after tumor cell grafting, the tumor necrosis factor α (TNF-α) and interferon γ (IFN-γ) cytokines were higher in the TOMM compared to the OOMM (Fig. 5A). TNF-α is mainly produced by activated macrophages and is a multi-functional pro-inflammatory cytokine that can activate T cells and stimulate their production of IFN-γ. The cytokines TNF-α and IFN-γ are recognized for a synergistic anti-tumor effect [18, 19]. The elevated levels of these cytokines in the traditional grafting model may contribute to the more rapid decline of surviving tumor cells in the traditional model compared to our optimized model. Additionally, the level of RANTES (CCL5) cytokines was higher in the improved model compared to the traditional model at 12 h and day 7. CCL5 expression is regulated by the STING signaling pathway, and recent literature suggests that the STING signaling pathway is related to dormant metastatic tumors [20]. The above results suggest that in the improved model, tumor cells entering the brain to some extent entered a dormant state and resumed proliferation after the inflammation caused by modeling subsided.

Astrocytes and microglia are the first to respond to inflammation in the brain, and the morphology of astrocytes and microglia represents their cellular function. To determine the impact of the two different models on the complexity of neuroglial cells, we evaluated the morphology of microglia and astrocytes around tumor cells 48 h after injecting tumor cells in the two models, using anti-Iba-1 staining for microglia and anti-GFAP staining for astrocytes (Fig. 5B). Consistent with previous reports, we found that under inflammatory conditions, astrocytes changed from small cell bodies with long and thin branches to cells with increased and thickened branches and enlarged cell bodies; microglia changed from cells with many branches extending to thin cell bodies to amoeba-like cells with fewer branches [21]. We then used Sholl analysis to analyze the complexity of astrocytes and microglia. We found that Sholl plots, which depict the number of interactions per 10 μm steps from the cell soma, GFAP + cell interactions were obviously reduced in the OOMM at 140 μm (Fig. 5C, D), and Iba-1 + cell interactions per 10 μm steps from the cell soma were reduced in the traditional method at 190 μm (Fig. 5E, F). These results suggest that the two models have different impacts on the neuroglial. The observed morphological changes in astrocytes and microglia indicate an activated

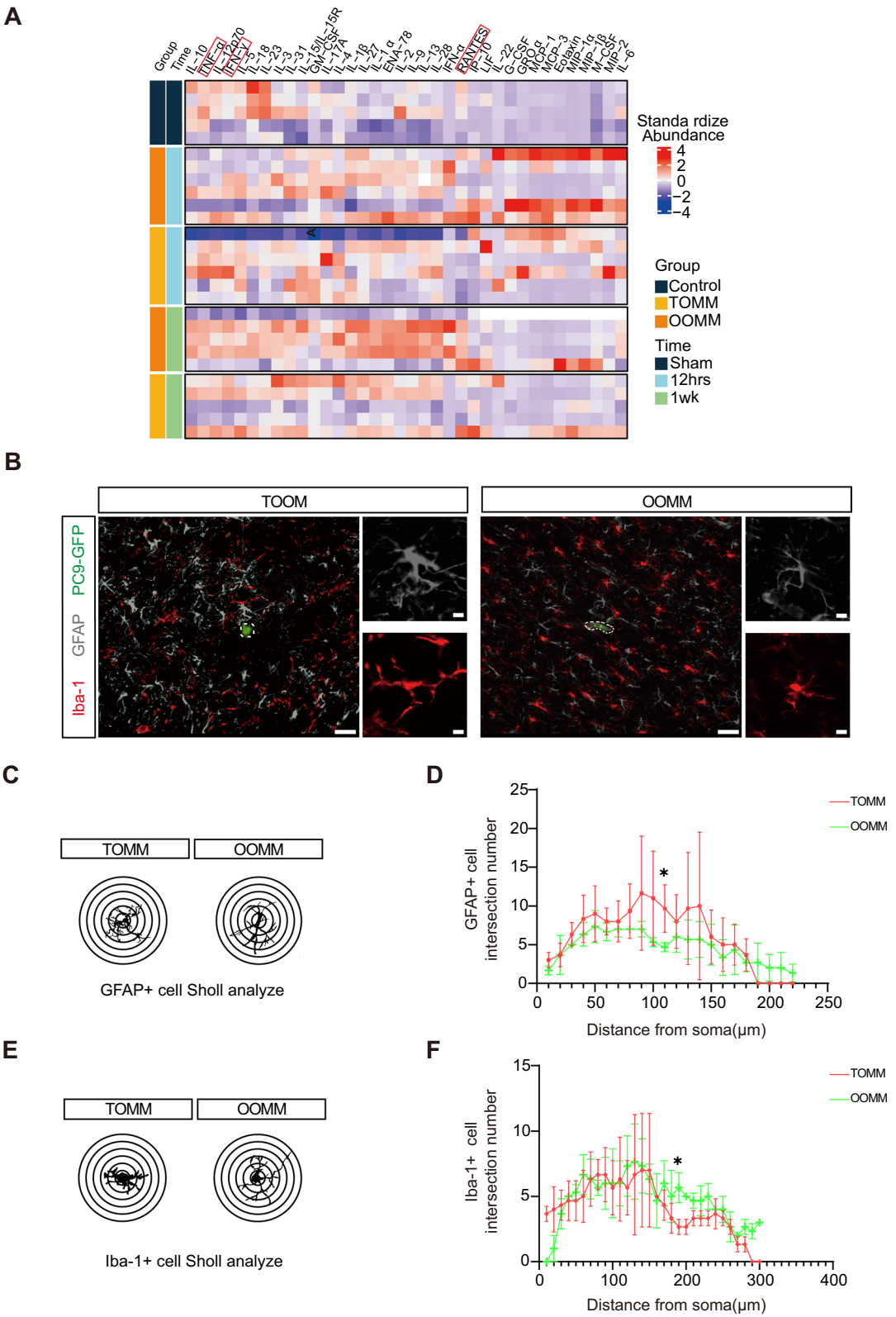
A
Group
Time
IL-10
TNF-α
IL-12p70
IFN-γ
IL-18
IL-23
IL-31
IL-5/IL-15R
GM-CSF
IL-17A
IL-4
IL-1β
IL-27
IL-1α
ENA-78
IL-2
IL-9
IL-13
IL-28
IFN-α
RANTES
IP-10
LIF
IL-22
G-CSF
GRO-α
MCP-1
MCP-3
Eotaxin
MIP-1α
MIP-1β
M-CSF
MIP-2
IL-6
Standa rdize Abundance
4
2
0
−2
−4
Group
Control
TOMM
OOMM
Time
Sham
12hrs
1wk
B
TOOM
OOMM
PC9-GFP
GFAP
Iba-1
C
TOMM
OOMM
GFAP+ cell Sholl analyze
D
GFAP+ cell intersection number
Distance from soma(μm)
TOMM
OOMM
E
TOMM
OOMM
Iba-1+ cell Sholl analyze
F
Iba-1+ cell intersection number
Distance from soma(μm)
TOMM
OOMM

◂**Fig. 5** Reduced brain inflammation and astrocyte and microglia activation post OOMM procedure compared to TOMM. **A** The level of inflammation-related cytokines in the mouse brain at 12 hour and one week following TOMM, OOMM, or sham surgery. **B** Representative GFAP staining and IBA-1 staining in brain tissue of mice harvested 12 h post the TOMM or OOMM procedure. Scale bar: left column 250 μm, right column 50 μm. $n = 3$ mice. **C** Two-dimensional Sholl analysis of GFAP + astrocytes in the superior frontal cortex of the brain from mice harvested 12 h post the TOMM or OOMM procedure. **D** The process intersections number of astrocytes from mice harvested 12 h post the TOMM or OOMM procedure. Data are presented as mean ± SD from $n = 3$ mice. * < 0.05 by paired t test. **E** Two-dimensional Sholl analysis of IBA-1 + microglia in the of the brain from mice harvested 12 h post the TOMM or OOMM procedure. **F** The process intersections number of microglia from mice harvested 12 h post the TOMM or OOMM procedure. Data are presented as mean ± SD from $n = 5$ mice. * < 0.05 by paired t test

state in TOMM, which is typically characterized by changes in cell size and branching complexity. In the OOMM group, astrocytes exhibited a star-like shape with multiple branches, and microglial cells displayed extended, fine branches stemming from a small core, indicating low inflammatory and cell resting states.

OOMM model enables multiple injections through the common carotid artery

Lung cancer brain metastasis is a complex process that includes lung cancer cells separating from the primary site, continuously falling from the primary site, and infiltrating through the blood and lymphatic systems, then entering the circulatory system, circulating tumor cells crossing the BBB to colonize and domesticate microenvironment cells in the brain's unique microenvironment. However, there is currently no model that can realistically simulate the entire process of lung cancer brain metastasis. The current lung cancer brain metastasis CCA injection model requires puncture on the CCA, and to prevent tumor cell reflux and bleeding, permanent closure of the CCA is necessary. This results in a one-time stimulation of the brain microenvironment by lung cancer cells, which fails to accurately replicate the repeated stimulation of the brain microenvironment by circulating tumor cells.Therefore, we developed a multiple injection model based on the OOMM, utilizing the CCA previously repaired by light-controlled hydrogel for repeated injections of lung cancer cells. The multiple injection process involves the first injection of a small amount of tumor cells to simulate the entry of circulating tumor cells into the brain circulation and the conditioning of the pre-metastatic microenvironment. After day 7 following the first injection, a second injection of tumor cells is performed to simulate the process by which subsequently circulating tumor cells rapidly adapt to and colonize the pre-metastatic microenvironment that has already been established. To explore the optimal cell concentration for conditioning the pre-metastatic microenvironment, we set three cell concentration gradients for the first injection: 2×10^4, 5×10^4, and 1×10^5. The second injection was performed with the same cell concentration as used in the TOMM and OOMM models. (Fig. 6A, B). After the first injection, the injection site was sealed using hydrogel. Seven days later, upon reopening the previous surgical site, it was observed that the previously implanted bioprotein gel remained intact. Following the second injection, the injection site was once again sealed using the light-controlled hydrogel (Fig. 6C). To ensure the detection of micro metastatic foci, we sectioned the entire mouse brain and performed H&E staining on all slices, followed by 3D reconstruction to observe and count the formation of all metastatic niches (Fig. 6D). The locations of the tumors within the brain were meticulously recorded, and whole-brain 3D reconstruction technology was utilized to accurately depict the spatial distribution of the tumors in the brain (Fig. 6E). We found that the number of brain metastatic tumors with multiple injection was higher than that in the group with OOMM, and the difference in the number of tumors between the two groups was statistically significant. However, there was no statistically significant difference in the number of tumors among the different cell concentration groups in the multiple injection group (Fig. 6F).

Exploring the role of circulating tumor cell in modulating pre-metastatic microenvironment

We investigated the differences in shaping the pre-metastatic microenvironment by a small number of circulating tumor cells (CTCs) versus a large number of CTCs. We performed immunofluorescence staining on brain tissue samples from mice in the multiple injection and OOMM groups at day 7 post-surgery. Notably, the multiple injection group was harvested after only the first injection of a small number of tumor cells. Astrocytes were stained with GFAP antibodies, and microglia were stained with Iba-1 antibodies. Staining results showed that in the OOMM group, both astrocytes and microglia were clustered around the tumor cells; however, in the multiple injection group, only astrocytes clustered around the tumor cells (Fig. 7A). We found that GFAP + cell interactions was obviously increasing in the multiple injection models at 60 μm (Fig. 7B), and Iba-1 + cell interactions per 10 μm steps from the cell soma were reduced in the traditional method at 70 μm (Fig. 7C). The statistical results revealed that the density of astrocytes in the multiple injection model was significantly higher than in the OOMM (Fig. 7D). Conversely, the density of microglia in the multiple injection model was significantly lower compared to that in the OOMM (Fig. 7E). These results suggest that the pioneer circulating tumor cells in the multiple injection group condition astrocytes, creating a suitable environment for the subsequent arrival of tumor cells.

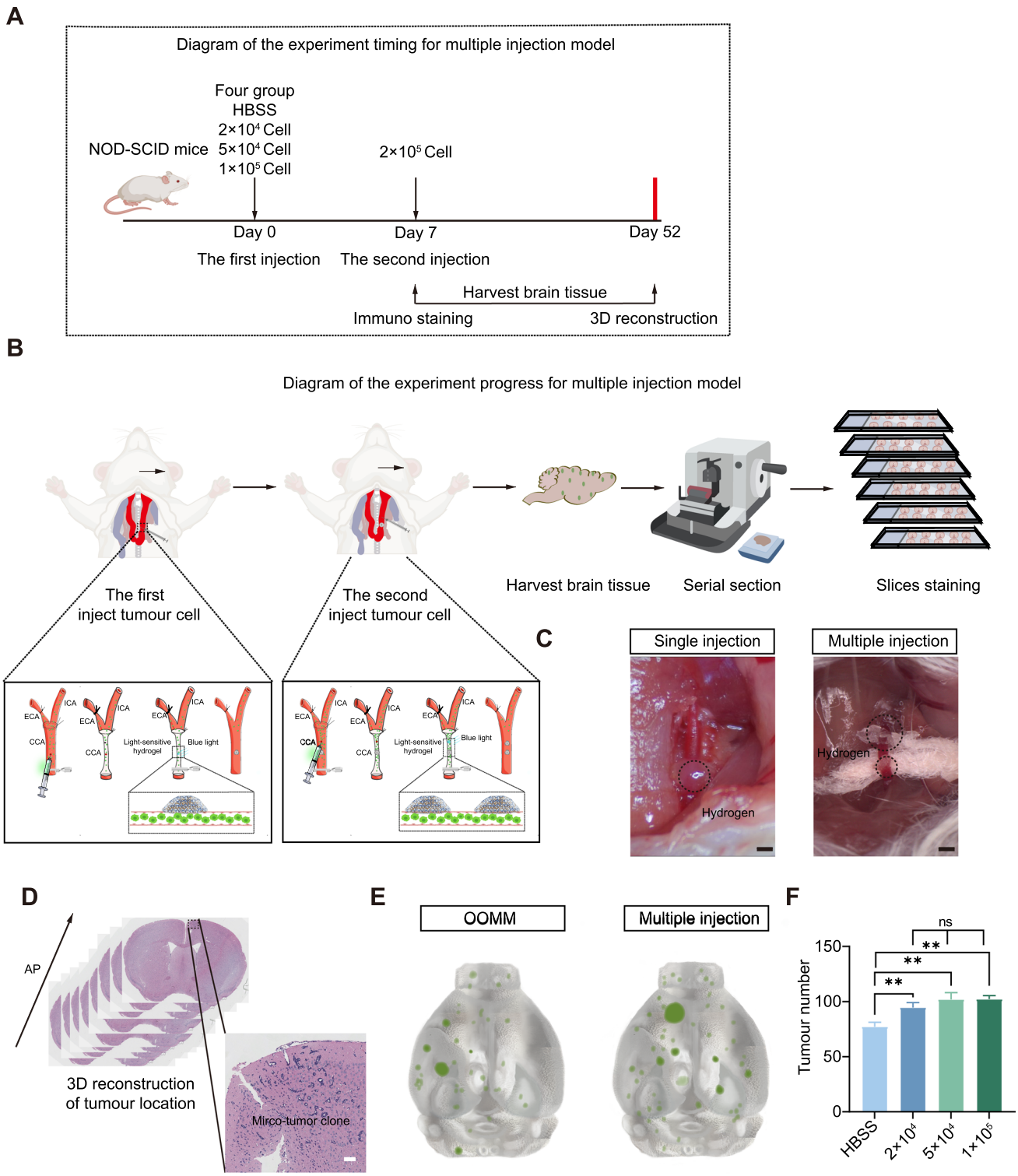
A
Diagram of the experiment timing for multiple injection model
Four group
HBSS
2×10⁴ Cell
5×10⁴ Cell
1×10⁵ Cell
NOD-SCID mice
2×10⁵ Cell
Day 0
Day 7
Day 52
The first injection
The second injection
Harvest brain tissue
Immuno staining
3D reconstruction
B
Diagram of the experiment progress for multiple injection model
The first inject tumour cell
The second inject tumour cell
Harvest brain tissue
Serial section
Slices staining
ECA
ICA
CCA
Light-sensitive hydrogel
Blue light
C
Single injection
Multiple injection
Hydrogen
D
AP
3D reconstruction of tumour location
Mirco-tumor clone
E
OOMM
Multiple injection
F
Tumour number
ns
**
HBSS
2×10⁴
5×10⁴
1×10⁵

◂**Fig. 6** OOMM enables multiple intracarotid injections. **A** Schematic diagram of the experiment for the multiple injection model to compare tumor formation numbers with different dose of cell in the first injection. **B** Schematic illustration of multiple tumor cell injections through the CCA in OOMM. **C** Images depicting the CCA after the first and the second injections. Scale bar: 2 mm. **D** Detection of tumor cells through DAPI staining of serially sectioned brain slides from mice treated with the multiple injection model and OOMM procedure. Scale bar: left column 2 mm, right column 250 μm. **E** 3D reconstruction of serially sectioned brain slides to depict the abundance, size, and location of tumor clones in mice treated with the multiple injection model and OOMM. **F** Quantification of the tumor numbers of different tumor cell numbers in OOMM and different group of the multiple model. Data are presented as mean ± SD from $n = 3$ mice. ** < 0.01 by one-way ANOVA

Discussion

The ongoing battle against lung cancer, particularly NSCLC, has been marked by significant advancements with targeted therapies and immunotherapies, enhancing patient prognosis [22]. Despite these advancements, the median survival time for patients with lung cancer brain metastasis remains distressingly limited, underscoring the urgent need for more effective treatment modalities and a comprehensive understanding of the underlying biological processes involved in brain metastasis [23].

The complexity of brain metastasis, characterized by a series of steps from the detachment of cancer cells from the primary tumor, their survival in the bloodstream, migration, and eventual colonization and establishment in the brain, presents a formidable challenge [24]. The intricacies of this metastatic process necessitate precise models for investigation, crucial for unraveling the cellular and molecular mechanisms underpinning Brain metastasis development and for the preclinical assessment of novel therapeutic strategies. However, the field has been hampered by the limitations of existing models, ranging from in vitro systems like cell cultures and 3D organoids to in vivo models including xenografts and genetically engineered mouse models [25]. Each model, while contributing valuable insights, falls short in fully replicating the multifaceted processes and conditions integral to brain metastasis.

In our quest to elucidate the intricacies of brain metastases stemming from NSCLC, a comprehensive examination was undertaken comparing traditional and modified in situ injection models. This investigation was primarily driven by the imperative to develop a model that more accurately simulates the cerebral microenvironment and the dynamics of tumor cell migration and survival within the brain. The modified model employed a novel approach using blue-light controlled bioprotein gel for the repair of the common carotid artery, which significantly restored blood flow and increased oxygen saturation by 60% in the left hemisphere of the mouse brain, compared to the traditional model that induced severe cerebral ischemia and hypoxia through permanent ligation of the artery.

This ischemic condition in the traditional model precipitated the widespread secretion of inflammatory factors, a phenomenon markedly mitigated in the modified model. This improvement in blood flow and oxygen saturation in the modified model resulted in significantly lower levels of pro-inflammatory cytokines, notably TNF-α and IFN-γ. This is pivotal, given the established role of inflammation in tumor progression and metastasis. The reduction in pro-inflammatory cytokines, such as TNF-α and IFN-γ, in the modified model aligns with current understanding of the inflammatory cascade's contribution to tumor cell survival and proliferation.The correlation between immune cell morphology and function was distinctly observed in the immunofluorescent staining of astrocytes and microglia, cells integral to the brain's immune defense. The traditional model activated these cells, as evidenced by the enlarged cell bodies and increased number of thickened processes in astrocytes, and the rounded cell bodies with short, thick processes in microglia, reflecting an ameboid-like deformation. In contrast, in the modified model, 12 h post-operation, showed only minimal activation of these cells.

Moreover, our research underscored the enhanced ability of the modified model to bolster tumor cell survival rates. At day 7 following the procedure, the survival rate of PC9 and A549 cells was noted to be approximately 27.87% and 46.25%, marking a statistically significant enhancement relative to the traditional model. This finding indicates that the cerebral microenvironment within the modified model offers a more favorable setting for the sustenance of tumor

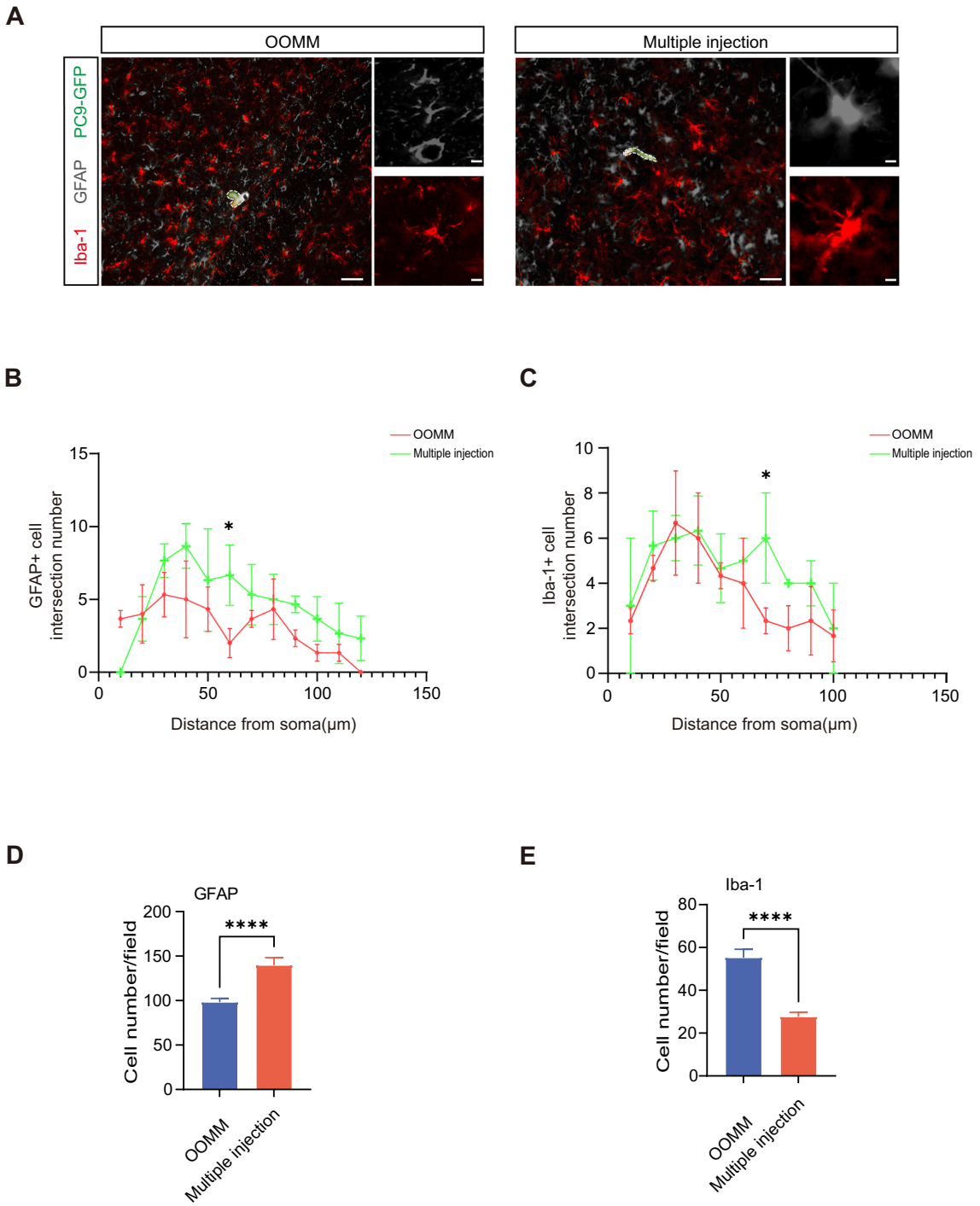

Fig. 7 Astrocyte active post multiple injection in OOMM. **A** Representative GFAP staining and IBA-1 staining of brain slides from mice at day 7 post the single injection or the multiple injection. **B** The number of process intersections of astrocyte from mice harvested day 7 post single injection or multiple injection procedure. Data are presented as mean ± SD from $n = 3$ mice. * < 0.05 by paired t test. **C** The process intersections number of microglia from mice harvested 7 days post the single injection or multiple injection procedure. Data are presented as mean ± SD from $n = 5$ mice. * < 0.05 by paired t test. **D**, **E** Counting the number of GFAP + signals (**D**) and IBA-1 signals (**E**) in brain tissue of mice at after 7 days treat with single injection and multiple injection. Data are presented as mean ± SD from $n = 3$ mice

cells. The traditional model, plagued by cerebral ischemia and hypoxia, may lead to a skewed understanding of tumor cell survival, reflecting an adaptation to ischemic conditions rather than the selective pressures exerted by the blood–brain barrier and the brain microenvironment. The ability of our modified model to accurately mimic the human disease process presents a transformative potential for cancer research and the development of therapeutics. This model serves as a distinct platform for examining the influence of pioneer tumor cells on the brain microenvironment, allowing for the observation of how these cells adapted to and primed the site for the invasion of subsequent tumor cells. Gaining insight into these preliminary phases of brain metastases could unveil effective strategies for impeding the onset of brain metastasis. Additionally, the model acts as an optimal venue for testing novel therapeutic agents, evaluating both their direct impacts on tumor cells and their capacity to penetrate the BBB and alter the brain's microenvironment. By enabling a thorough understanding of the underpinnings of metastasis and evaluating therapeutic approaches with elevated translational potential, this model lays the groundwork for innovatie therapeutic strategies. It effectively narrows the chasm between preclinical studies and clinical implementation, signaling the advent of a new phase in the clinical management of lung cancer patients, with the potential to substantially enhance patient outcomes.

Building upon the modified model, we ventured to establish a multi-tumor injection model to simulate the initial interaction of pioneer tumor cells with the blood–brain barrier and the brain microenvironment. Injecting tumor cells at lower concentrations (2×10^4, 5×10^4, 1×10^5 cells) aimed to mimic the stimulation provided by pioneer tumor cells. Comparing the microenvironmental impact seven days post-injection between low and high tumor cell concentrations revealed differential activation of astrocytes and microglia. Low concentration injections preferentially activated astrocytes without stimulating microglia, whereas high concentration injections activated both cell types. These findings underscore the importance of restoring proper cerebral blood supply to mitigate inflammation and improve the conditions for tumor cell survival within the brain. Furthermore, the differential activation of astrocytes and microglia observed in the multi-tumor injection model call attention to the fact that tumor microenvironment is dynamics. To manage or prevent brain metastasis, illustrating the role of astrocytes in pre-metastatic lesion is essential. The modified model presents a significant advancement in accurately simulating the cerebral microenvironment, offering a deeper understanding of the interplay between tumor cells, the blood–brain barrier, and brain immunity. The implications of these findings extend beyond the technical achievements, providing a foundation for future research into the development of targeted therapies that consider the complexity of brain metastases from NSCLC. This study not only contributes to the refinement of experimental models but also paves the way for novel therapeutic interventions aimed at combating one of the most challenging aspects of cancer treatment: the effective management of brain metastases.

In parallel, this study maybe provide a perspective on the implications of tyrosine kinase inhibitors (TKIs) on BBB integrity. TKIs, a cornerstone in the arsenal of targeted therapies for NSCLC, target multiple receptor tyrosine kinases including VEGFR, c-KIT, PDGFRβ, and EGFR [26, 27]. By inhibiting these kinases, TKIs block crucial signaling pathways for cancer cell proliferation but may also disrupt signaling pathways maintaining endothelial cell cohesion, potentially increasing BBB permeability [28, 29]. This dual action underscores the complexity of treating brain metastasis, necessitating a careful balance between targeting tumor cells and preserving BBB protective mechanisms. Utilizing our newly developed OOMM, future research could aim to evaluate and screen for pharmacological compounds that can mitigate the adverse effects of TKIs on the BBB. By identifying agents that can preserve the integrity of the BBB while maintaining the therapeutic efficacy of TKIs against tumor cells, we could aspire to develop a dual-action therapeutic strategy that not only inhibits tumor proliferation but also minimizes the risk of metastatic progression to the brain.

In conclusion, the OOMM represents a significant advancement in the modeling of brain metastasis, potentially bridging the gap between the translation of bench research into effective clinical treatments. By providing insights into the tumor microenvironment and factors influencing tumor cell survival, migration, and colonization in the brain, this model opens the door to novel therapeutic strategies and enhances our understanding of brain metastasis, ultimately aiming to improve patient outcomes in the fight against lung cancer.

Supplementary Information The online version contains supplementary material available at https://doi.org/10.1007/s10585-025-10336-3.

Acknowledgements None.

Authors contribution Zihao Liu, Huisheng Song, Zhenning Wang and Maojin Yao conceived the study. Zihao Liu performed the experiments and drafted the manuscript. Huisheng Song and Wenfeng Ning provided the financial support. Zhenning Wang supported the tumor injection and IF technique. Yang Hu supported stable cell transfection. Xiaoxuan Zhong, Yizhi Liang and Long Jin supported photoacoustic imaging technology. Huiling Liu supported light-controlled gelatin (GelMA/HAMA) and did the experiment for supplement Fig. 1. Zhiming Ye did the experiment for Fig. 5 A. Shengfang Yuan and Zijun Deng did the experiment for serial section. Jieying Mo helped checking all the typing in manuscript. Jianhao Zeng, Jiaoyan Ren and Maojin Yao supervised and revised the manuscript. All authors read and approved the final manuscript.

Funding This work was supported by the National Natural Science Foundation of China (No. 82072787), Sixth Affiliated Hospitalf Guangzhou Medical University, Qingyuan People's Hospital Medical Research Foundation (No.202301–207), the Tertiary Education Scientific Research Project of Guangzhou Municipal Education Bureau (No. 202235421), and the Special Funds for the Cultivation of Guangdong College Students' Scientific and Technological Innovation "Climbing Program" Special Funds (No. pdjh2024b313).

Availability of data and materials The data sets used in this study are available from the corresponding author upon request.

Declarations

Conflict of interest The authors declare no conflicts of interest.

Ethical approval The animal experiments in this study were approved by Guangzhou medical university committee for animal (No. 2023395).

Consent for publication All authors have consented to the publication of this manuscript.

References

1. Sperduto PW et al (2017) Estimating survival in patients with lung cancer and brain metastases: an update of the graded prognostic assessment for lung cancer using molecular markers (lung-molGPA). JAMA Oncol 3(6):827–831. https://doi.org/10.1001/jamaoncol.2016.3834
2. Lin X, DeAngelis LM (2015) Treatment of brain metastases. J Clin Oncol 33(30):3475–3484. https://doi.org/10.1200/JCO.2015.60.9503
3. Achrol AS et al (2019) Brain metastases. Nat Rev Dis Primers 5(1):5. https://doi.org/10.1038/s41572-018-0055-y
4. Bui N et al (2016) Novel treatment strategies for brain metastases in non-small-cell lung cancer. Curr Treat Options Oncol 17(5):25. https://doi.org/10.1007/s11864-016-0400-x
5. Lee HJ et al (2019) A large-scale analysis of targeted metabolomics data from heterogeneous biological samples provides insights into metabolite dynamics. Metabolomics 15(7):103. https://doi.org/10.1007/s11306-019-1564-8
6. Lazarczyk M et al (2023) The journey of cancer cells to the brain: challenges and opportunities. Int J Mol Sci. https://doi.org/10.3390/ijms24043854
7. Chambers AF, Groom AC, MacDonald IC (2002) Dissemination and growth of cancer cells in metastatic sites. Nat Rev Cancer 2(8):563–572. https://doi.org/10.1038/nrc865
8. Popper HH (2016) Progression and metastasis of lung cancer. Cancer Metastasis Rev 35(1):75–91. https://doi.org/10.1007/s10555-016-9618-0
9. Marozzi M et al (2021) Inflammation, extracellular matrix remodeling, and proteostasis in tumor microenvironment. Int J Mol Sci. https://doi.org/10.3390/ijms22158102
10. Quail DF, Joyce JA (2017) The microenvironmental landscape of brain tumors. Cancer Cell 31(3):326–341. https://doi.org/10.1016/j.ccell.2017.02.009
11. Hu Y et al (2023) The evolution of tumor microenvironment in gliomas and its implication for target therapy. Int J Biol Sci 19(13):4311–4326. https://doi.org/10.7150/ijbs.83531
12. Yuan Z et al (2023) Extracellular matrix remodeling in tumor progression and immune escape: from mechanisms to treatments. Mol Cancer 22(1):48. https://doi.org/10.1186/s12943-023-01744-8
13. Follain G et al (2018) Hemodynamic forces tune the arrest, adhesion, and extravasation of circulating tumor cells. Dev Cell 45(1):33–52. https://doi.org/10.1016/j.devcel.2018.02.015
14. Kurian AG et al (2022) Multifunctional GelMA platforms with nanomaterials for advanced tissue therapeutics. Bioact Mater 8:267–295. https://doi.org/10.1016/j.bioactmat.2021.06.027
15. Zhang G et al (2023) Engineered dermis loaded with confining forces promotes full-thickness wound healing by enhancing vascularisation and epithelialisation. Acta Biomater 170:464–478. https://doi.org/10.1016/j.actbio.2023.08.049
16. Zhang Q et al (2021) Photo-crosslinkable amniotic membrane hydrogel for skin defect healing. Acta Biomater 125:197–207. https://doi.org/10.1016/j.actbio.2021.02.043
17. Fan Y et al (2020) Hybrid printing using cellulose nanocrystals reinforced GelMA/HAMA hydrogels for improved structural integration. Adv Healthc Mater 9(24):e2001410. https://doi.org/10.1002/adhm.202001410
18. Wu L et al (2023) Tumor aerobic glycolysis confers immune evasion through modulating sensitivity to T cell-mediated bystander killing via TNF-alpha. Cell Metab 35(9):1580–1596. https://doi.org/10.1016/j.cmet.2023.07.001
19. Boulch M et al (2023) Tumor-intrinsic sensitivity to the pro-apoptotic effects of IFN-gamma is a major determinant of CD4(+) CAR T-cell antitumor activity. Nat Cancer 4(7):968–983. https://doi.org/10.1038/s43018-023-00570-7
20. Hu J et al (2023) STING inhibits the reactivation of dormant metastasis in lung adenocarcinoma. Nature 616(7958):806–813. https://doi.org/10.1038/s41586-023-05880-5
21. Nordengen K et al (2019) Glial activation and inflammation along the Alzheimer's disease continuum. J Neuroinflammation 16(1):46. https://doi.org/10.1186/s12974-019-1399-2
22. Hirsch FR et al (2017) Lung cancer: current therapies and new targeted treatments. Lancet 389(10066):299–311. https://doi.org/10.1016/S0140-6736(16)30958-8
23. Mok TSK et al (2017) The accelerated path of ceritinib: translating pre-clinical development into clinical efficacy. Cancer Treat Rev 55:181–189. https://doi.org/10.1016/j.ctrv.2017.03.006
24. Valastyan S, Weinberg RA (2011) Tumor metastasis: molecular insights and evolving paradigms. Cell 147(2):275–292. https://doi.org/10.1016/j.cell.2011.09.024
25. Liu Z et al (2024) Experimental models for cancer brain metastasis. Cancer Pathog Ther 2(1):15–23. https://doi.org/10.1016/j.cpt.2023.10.005
26. Yuan M et al (2019) The emerging treatment landscape of targeted therapy in non-small-cell lung cancer. Signal Transduct Target Ther 4:61. https://doi.org/10.1038/s41392-019-0099-9
27. Esteban-Villarrubia J et al (2020) Tyrosine kinase receptors in oncology. Int J Mol Sci. https://doi.org/10.3390/ijms21228529
28. Chen J et al (2017) A role for ErbB signaling in the induction of reactive astrogliosis. Cell Discov 3:17044. https://doi.org/10.1038/celldisc.2017.44

29. Manu DR et al (2023) Astrocyte involvement in blood-brain barrier function: a critical update highlighting novel, complex, neurovascular interactions. Int J Mol Sci. https://doi.org/10.3390/ijms242417146

Authors and Affiliations

Zihao Liu[1] · Huisheng Song[2] · Zhenning Wang[3] · Yang Hu[1] · Xiaoxuan Zhong[4] · Huiling Liu[5] · Jianhao Zeng[6] · Zhiming Ye[1] · Wenfeng Ning[7] · Yizhi Liang[4] · Shengfang Yuan[1] · Zijun Deng[1] · Long Jin[4] · Jieying Mo[1] · Jiaoyan Ren[8] · Maojin Yao[1]

✉ Maojin Yao
yaomaojin@gird.cn

1 State Key Laboratory of Respiratory Disease, National Clinical Research Center for Respiratory Disease, National Center for Respiratory Medicine, Department of Thoracic Surgery and Oncology, Guangzhou Institute of Respiratory Health, The First Affiliated Hospital of Guangzhou Medical University, Guangzhou 510182, Guangdong, People's Republic of China

2 The Affiliated Qingyuan Hospital (Qingyuan People's Hospital), Guangzhou Medical University, Qingyuan 511518, Guangdong, China

3 Department of Neurosurgery, The Tenth Affiliated Hospital, Southern Medical University (Dongguan People's Hospital), Dongguan 523059, China

4 Guangdong Provincial Key Laboratory of Optical Fiber Sensing andCommunication, Institute of Photonics Technology, College of Physics & Optoelectronic Engineering, Jinan University, Guangzhou 510632, China

5 Key Laboratory of Biomaterials of Guangdong Higher Education Institutes, Guangdong Provincial Engineering and Technological Research Center for Drug Carrier Development, Department of Biomedical Engineering, Jinan University, Guangzhou 510632, Guangdong, China

6 Department of Microbiology, Immunology, and Cancer Biology, University of Virginia Health System, Charlottesville, VA 22908, USA

7 Ningyuan County People's Hospital, Yongzhou 425699, Hunan, China

8 School of Food Sciences and Engineering, South China University of Technology, Guangzhou 510641, China